JACS
JOURNAL OF THE AMERICAN CHEMICAL SOCIETY
pubs.acs.org/JACS
Article

# Confining and Highly Dispersing Single Polyoxometalate Clusters in Covalent Organic Frameworks by Covalent Linkages for $CO_2$ Photoreduction

Meng Lu, Mi Zhang, Jiang Liu, Tao-Yuan Yu, Jia-Nan Chang, Lin-Jie Shang, Shun-Li Li, and Ya-Qian Lan*

Cite This: *J. Am. Chem. Soc.* 2022, 144, 1861−1871
Read Online



**ABSTRACT:** Single clusters have attracted extensive research interest in the field of catalysis. However, achieving a highly uniform dispersion of a single-cluster catalyst is challenging. In this work, for the first time, we present a versatile strategy for uniformly dispersed polyoxometalates (POMs) in covalent organic frameworks (COFs) through confining POM cluster into the regular nanopores of COF by a covalent linkage. These **COF-POM** composites combine the properties of light absorption, electron transfer, and suitable catalytic active sites; as a result, they exhibit outstanding catalytic activity in artificial photosynthesis: that is, $CO_2$ photoreduction with $H_2O$ as the electron donor. Among them, **TCOF-MnMo$_6$** achieved the highest CO yield (37.25 $\mu$mol g$^{-1}$ h$^{-1}$ with ca. 100% selectivity) in a gas−solid reaction system. Furthermore, a mechanism study based on density functional theory (DFT) calculations demonstrated that the photoinduced electron transfer (PET) process occurs from the COF to the POM, and then $CO_2$ reduction and $H_2O$ oxidation occur on the POM and COF, respectively. This work developed a method for a uniform dispersion of POM single clusters into a COF, which also shows the potential of using **COF-POM** functional materials in the field of photocatalysis.

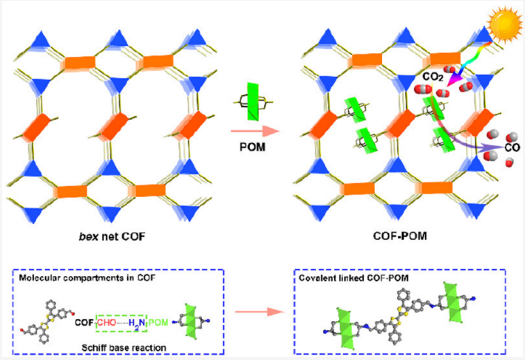


## ■ INTRODUCTION

Cluster, as an important intermediate component between single atom and nanoparticle, has been regarded as one of the most attractive catalysts.[1−3] Metal clusters, including coinage-metal clusters, polyoxometalate clusters, metal halide clusters, metal sulfide clusters, metalloid clusters and so on, have been widely studied.[4−7] Similar to the concept of single-atom catalysts (SACs) with isolated single metal atoms embedded within a solid matrix,[8] single-cluster catalysts (SCCs) can be considered to be the isolated distribution of single clusters on supports. SCCs usually showed enhanced activity and designated selectivity in catalysis because of their well-defined electronic and geometric structures.[9] Furthermore, due to the accurate atomic composition of the cluster, it is easier to study the relationship between structure and function in catalysis.[10] Many works have revealed that SACs combine the advantages of both homogeneous and heterogeneous catalysts and therefore exhibit high activity and selectivity in the catalytic process.[8,11−13] In comparison with SACs, SCCs not only possess the above features but also provide multielectron transfer and synergistic catalytic activity, which is conducive to conducting more complex reactions.[14] However, SCCs still face many problems such as poor stability, low surface area, a tendency to aggregate during the catalytic process, and so on, thereby significantly reducing their activity. In order to solve the above issues, an excellent idea is to integrate them with supports,[8,15] such as carbon nanotubes, graphene, and organic polymers, to form hybrid catalytic materials.[16,17] However, the uniform loading and dispersing of clusters in these disordered materials is difficult and also causes instability because of the weak interaction force. In addition, integrating clusters with crystalline porous complexes such as metal−organic frameworks (MOFs) or metal−organic cages (MOCs) can solve the problem of uniform dispersion, while the overall stability is still unresolved. In comparison with electrostatic interactions, van der Waals forces, hydrogen bonding, and coordination bonding, it is recognized that covalent bonding is the most stable.[4,8,18] On the basis of the functionalization of the cluster, achieving a high uniform dispersion and a highly stable covalent connection of SCCs on supports simultaneously is challenging. In this work, on the basis of a typical metal cluster,

**Received:** November 16, 2021
**Published:** January 20, 2022







https://doi.org/10.1021/jacs.1c11987
*J. Am. Chem. Soc.* 2022, 144, 1861−1871

**Scheme 1. Schematic Representation of Uniformly Dispersed POM Clusters in COF by Confining Them into the Pores of COF through Covalent Linkages.**

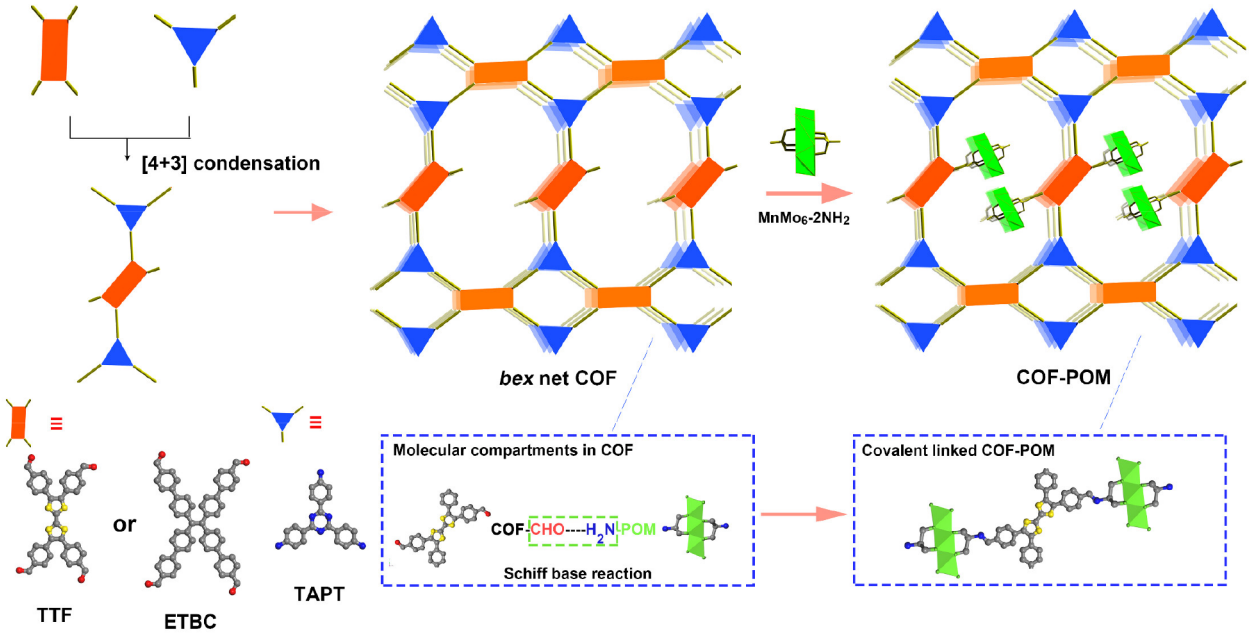


namely polyoxometalate (POM) cluster as a study model, we developed a general method to meet the above demands.

POMs with rich redox activity, adjustable structure, and extensive tunability have shown great potential in photocatalysis,[19] such as water splitting,[20−23] the $CO_2$ reduction reaction ($CO_2RR$),[24−29] $N_2$ fixation,[30] organic molecular transformation,[31,32] etc.[33] However, a bulk POM as a photocatalyst usually has poor stability, low light absorption ability, low specific surface area, etc.[33,34] Considering that most POM single clusters have a sub-nanometer size,[4] we believe that dispersing them into highly ordered crystalline and functional materials would be an ideal way to overcome the above issues.[9,35,36] Covalent organic frameworks (COFs), a class of newly developed crystalline materials with flexible structural designability and high stabilities,[37] also have a periodic skeleton and nanometer-size pores[38−40] are promising platforms for anchoring a sub-nanometer sized cluster.[41−43] More importantly, the functionalized organic skeleton of COF provides felicitous conditions for realizing a covalent link. However, such SCCs and design methods have not been reported. It is a crucial issue to realize the uniform dispersion and effective grafting of POM clusters in COF simultaneously.

Herein, we developed a general strategy to confine POM single clusters in the nanopores of crystalline COFs via covalent linkage. We rationally designed two subvalent COFs (TTF-TAPT COF and ETBC-TAPT COF, abbreviated as **TCOF** and **ECOF**) by condensing tri- and tetratopic linkers to form imine-linked [4 + 3] COFs with *bex* net topology,[44−46] and the periodic uncondensed aldehyde functionalities in the pores can be used for subsequent reactions with the amine-functionalized POM ($MnMo_6$-$2NH_2$)[47,48] by using a Schiff base reaction to achieve covalent bonding between them (named **COF-POM**, Scheme 1) and generate molecular compartments. This method realized the stable confinement of POMs in COF nanopores by covalent linkages, also achieving the high dispersion of POM single clusters in the overall COF materials.

In these **COF-POM** structures, the porous COF not only plays a role of a support but also possesses light absorption and $CO_2$ enrichment ability itself. In addition, the highly dispersed $MnMo_6$ clusters can act as active sites for catalytic $CO_2$ reduction, and the covalent bond is able to enhance electron transfer efficiency. As a result, the synthesized TTF-TAPT COF-$MnMo_6$ and ETBC-TAPT COF-$MnMo_6$ (abbreviated as **TCOF-$MnMo_6$** and **ECOF-$MnMo_6$**) combine the properties of light absorption, electron transfer, and a suitable band gap and active sites for visible-light catalytic $CO_2$ reduction. The covalently linked **TCOF-$MnMo_6$** catalyst showed the highest CO production rate of 37.25 $\mu$mol $g^{-1}$ $h^{-1}$ in a gas−solid $CO_2$ reduction reaction, which is at the forefront of the reported POM- and COF-based catalysts. Furthermore, density functional theory (DFT) calculations demonstrated that a photoinduced electron transfer (PET) process occurred from the COF to the POM then performed $CO_2$ reduction and $H_2O$ oxidation on POM and COF, respectively. This is the first report of covalently bonded **COF-POM** composites for photocatalysis, and it is also of great significance in the field of high dispersion of isolated single-cluster catalysts.

## ■ RESULTS AND DISCUSSION

**Synthesis and Structure of Subvalent COF.** As shown in Figure 1, a [4 + 3] condensation reaction was applied to synthesize a subvalent COF. Specifically, **TCOF** was synthesized by a Schiff-base condensation between 2,3,6,7-tetrakis(4-formylphenyl)tetrathiafulvalene (TTF-4CHO) and 2,4,6-tris(4-aminophenyl)-1,3,5-triazine (TAPT) by a solvothermal method (Figure 1a−c). The formation of a Schiff base linkage in **TCOF** was first confirmed by solid-state $^{13}C$ cross-polarization magic angle spinning ($^{13}C$ CP/MAS) NMR spectroscopy (Figure 1d) and Fourier transform infrared spectroscopy (FTIR) (Figure 2c). The peak at 159 ppm (1 in Figure 1d) in $^{13}C$ CP/MAS NMR was attributed to the C of the imine bond.[49] The appearance of a new peak at 1625 $cm^{-1}$ in the Fourier transform infrared (FTIR) spectrum can be


https://doi.org/10.1021/jacs.1c11987
J. Am. Chem. Soc. 2022, 144, 1861−1871

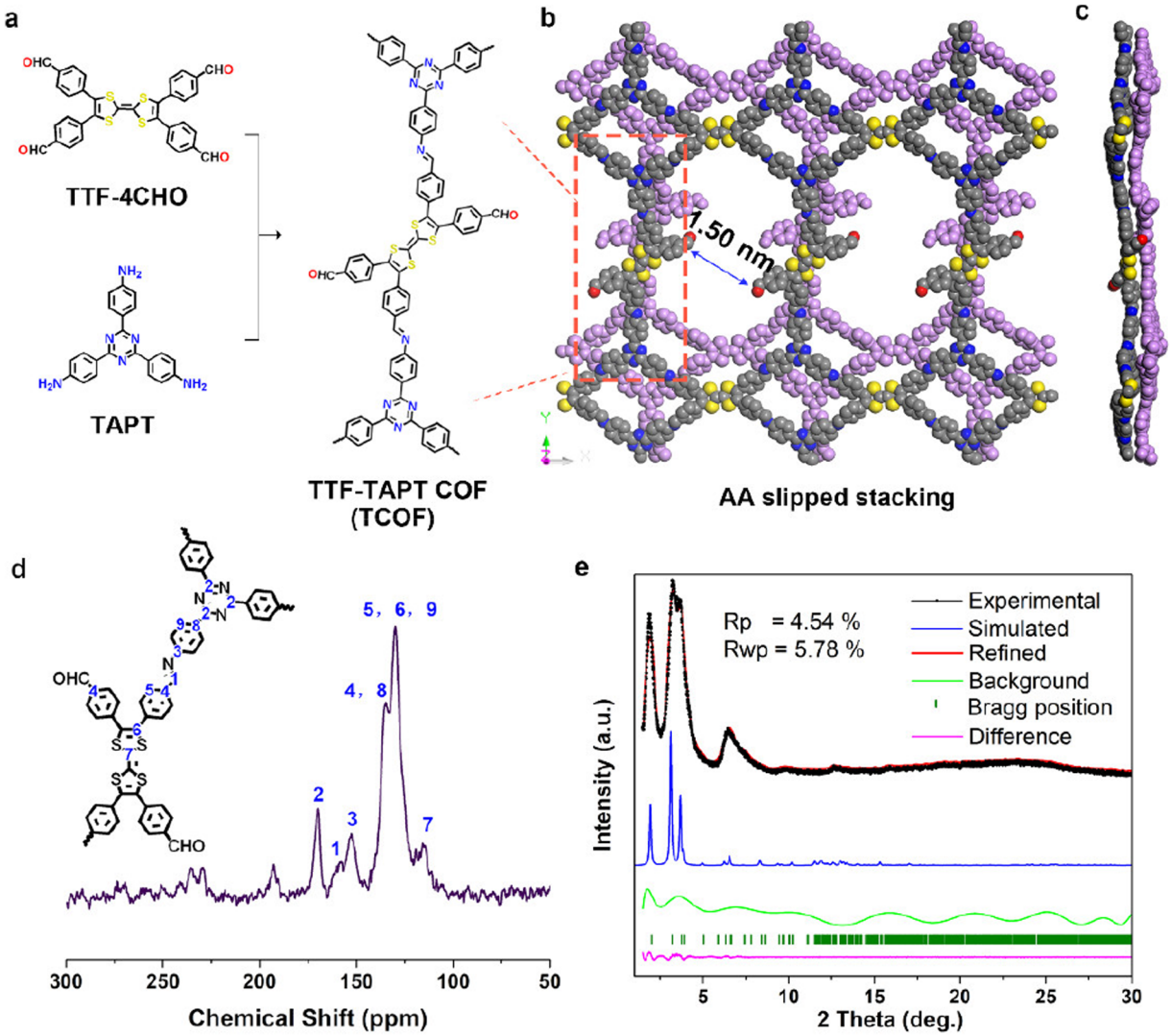


**Figure 1.** Structure and characterization of **TCOF**. (a) Synthesis of **TCOF**. (b) Top view and (c) side view of the slipped AA stacking structure of **TCOF** based on PXRD and modeling. (d) $^{13}$C CP/MAS NMR spectrum of TCOF. The assignments of $^{13}$C chemical shifts of **TCOF** are indicated in the chemical structure. (e) Experimental, simulated, and Pawley refined PXRD of the **TCOF** crystal structure on the basis of the AA slipped stacking models.

assigned to the telescopic vibration of an imine bond (−C═N).[50] All of these results confirmed the successful condensation reaction resulting in **TCOF**.

The crystal structure of **TCOF** was determined by powder X-ray diffraction (PXRD) combined with a theoretical structural simulation using the Materials Studio package. An AA (eclipsed) stacking model, an AB (staggered) stacking model, and an AA slipped stacking model based on **TCOF** were built (Section S3 (Structural Modeling) in the Supporting Information). The experimental PXRD diffraction patterns matched well with the calculated results from the AA slipped stacking mode, while a comparison of the other two showed significant deviations (Figure S46). We then carried out Pawley refinements of the PXRD patterns for full profile fitting against the proposed AA slipped stacking models, which provided unit cell parameters of $a$ = 29.1977 Å, $b$ = 48.9190 Å, $c$ = 7.7369 Å, $\alpha$ = 69.0851°, $\beta$ = 75.6574°, and $\gamma$ = 84.7350°. The refinement of PXRD diffraction patterns fitted well with the experimental results, with residuals of $R_p$ = 4.54% and $R_{wp}$= 5.78% (Figure 1e). **TCOF** exhibited diffraction peaks at 3.10, 3.57, and 6.33°, which were assigned to the (100), (020), and (200) planes, respectively. The simulated crystal structure showed that the pore size of **TCOF** is ∼1.5 nm (Figure 1b). We also synthesized **ECOF** with a structure similar to that of **TCOF** (Figure S1), and the details of the synthetic procedure and characterization are provided in the Section S1.1 in the Supporting Information.

**Synthesis and Structure of COF-POMs.** According to the method presented in Scheme 1, we successfully synthesized two covalent-linked **COF-POMs**, named **TCOF-MnMo$_6$** and **ECOF-MnMo$_6$** (For more details, please see Section S1.1 and Figures S2 and S3 in the Supporting Information). The highly ordered, periodic structure of the COF-POMs was characterized by high-resolution transmission electron microscopy (HR-TEM, Figure. 2a), FFT images (Figure. 2b) and its inverse fast Fourier transform (IFFT) images (Figure 2c). As shown in the HR-TEM and IFFT images, the MnMo$_6$ units can be identified as bright spots, while the components of COFs were identified as slightly darker spots. The honeycomb-shaped dark areas adjacent to the bright spots and the dimmer


https://doi.org/10.1021/jacs.1c11987
J. Am. Chem. Soc. 2022, 144, 1861−1871

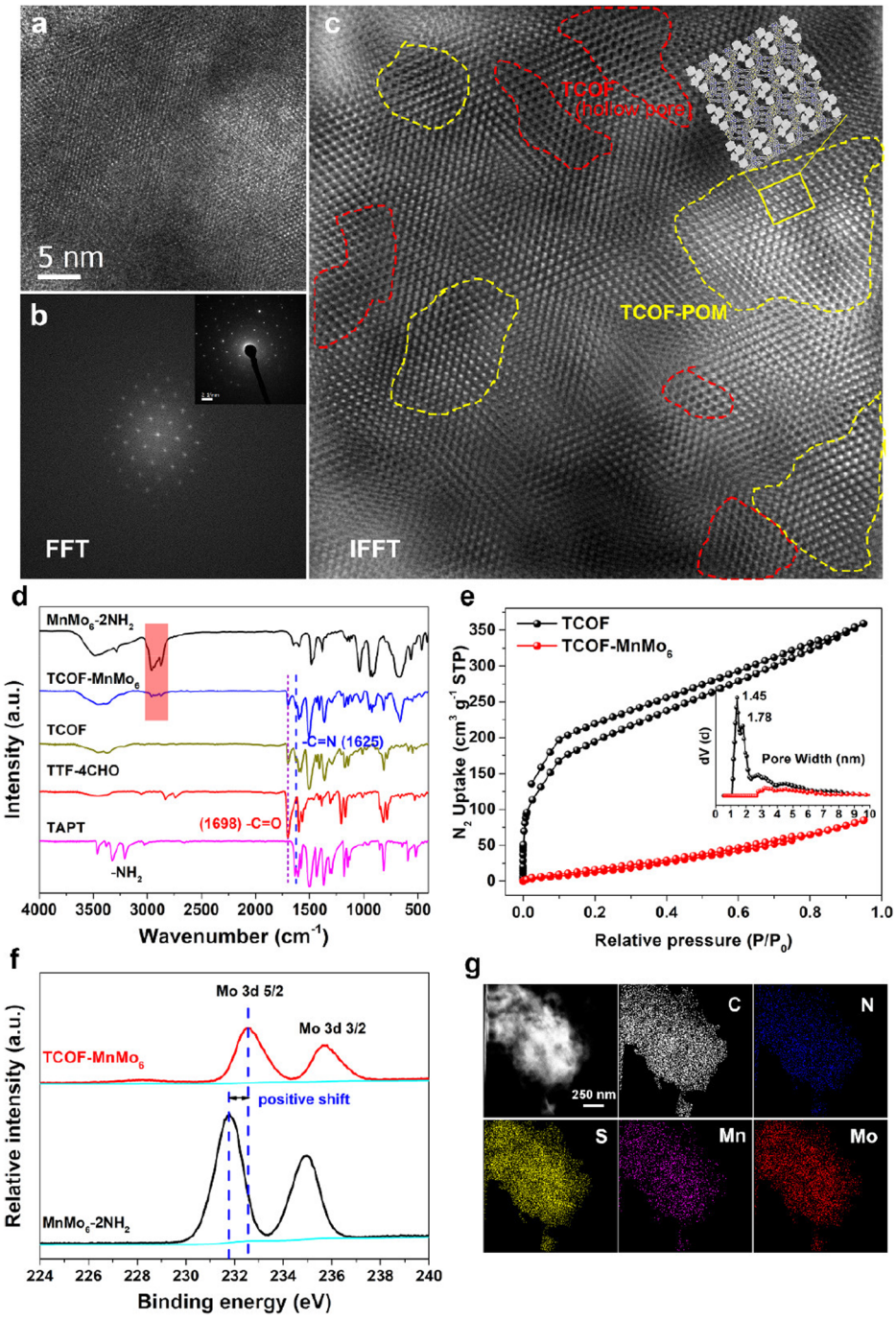


**Figure 2.** (a) HR-TEM image of **TCOF-MnMo$_6$**. (b) Fast Fourier transform of HR-TEM. Inset: selected area electron diffraction (SAED) pattern. (c) IFFT image of the HR-TEM. (d) Comparison of the FTIR spectra of **TCOF**, **TCOF-MnMo$_6$**, and the corresponding building units. (e) Comparison of $N_2$ adsorption isotherms of **TCOF** and **TCOF-MnMo$_6$** at 77 K and a graph of the pore-size distribution. (f) Comparison of XPS spectra of **TCOF-MnMo$_6$** and MnMo$_6$-2NH$_2$. (g) Annular-dark-field EDX element mapping of **TCOF-MnMo$_6$**.

spots correspond to the pore space in the **COF-POM**s. It is noted that vertical, parallel, and tilted arrays of structures coexist in the HRTEM; here we only focus on the vertical sights (view in the *ab* plane direction): i.e. we can visualize the pore structure of the COF. However, only a small proportion of the 2D-COF crystals was placed in this orientation. The IFFT microscopy images clearly showed that POMs (bright spots) were immobilized in the pore of the COF (highlighted in a yellow frames). It can also be observed that not all of the pores were occupied by MnMo$_6$ from the enlarged IFFT image; some hollow pores still exist, as shown in Figure 2c, highlighted in red frames. This is consistent with the actual content of MnMo$_6$ in **TCOF-MnMo$_6$**, which we calculated from ICP and TGA analysis. Furthermore, the periodic structural features in the HR-TEM images are consistent with those of the experimental unit cell. The crystal structure of **TCOF-MnMo$_6$** is shown as a highlighted diagram which is overlaid with the HR-TEM image. We also synthesized samples by the simple inclusion of POM clusters within the pores of COFs without covalent linkages (named **POM@**


https://doi.org/10.1021/jacs.1c11987
J. Am. Chem. Soc. 2022, 144, 1861−1871

**COF**) by using the $MnMo_6$ (without a $-NH_2$ functional group) cluster as the starting material. The HR-TEM results showed that only a small amount of POM cluster was confined in the COF pores in **POM@COF** (Figure S4; the bright dots in the area are circled by yellow dashes), while most of the ranges are hollow pores of the COF.

We then performed a high-resolution high-angle annular dark field-scanning transmission electron microscopy (HAADF-STEM) characterization; these results directly show that the POM cluster is distributed in the COF framework (bright spots in Figure S5a, while pure **TCOF** only shows homogeneous and smooth sheets, Figure S5b). It is noted that the distance between two adjacent spots is ∼2.8 nm, which is finely matched with the value calculated from the theoretical structure (Figure S5c). The regular array arrangement conforms to the proposed results: that is, the POM is uniformly loaded in the regular pores in the COF. In order to further distinguish the exact location of the POM compound in COF pores, we further performed an AC-TEM (spherical aberration corrected transmission electron microscope) test and expected to get higher resolution images; unfortunately, after many attempts, we ultimately did not obtain clear images. We think this is due to the fact that the **TCOF-MnMo$_6$** structure is sensitive to high energy electron beams and thus rapidly loses its crystallinity, making it difficult to obtain high-resolution images.

For **ECOF-MnMo$_6$**, as displayed in Figure S6, POM single clusters are highly dispersed in the **ECOF** platform but did not form a regular arrangement. This is due to the fact that **ECOF** has an AB stacked structure[45] and the steric hindrance in the pore environment blocked the effective confinement of POM clusters. In addition, we also performed FTIR, $N_2$ adsorption, pore size distribution, XPS, and EDX element mapping characterizations to confirm the structure of **COF-POM**. Detailed FTIR tests were performed to characterize the chemical structure of **TCOF** and **TCOF-MnMo$_6$**, which showed that the −C═O stretching vibration band at 1698 $cm^{-1}$ belonged to an uncondensed aldehyde group in TTF-4CHO of TCOF that obviously decreased (Figure 2d and Figure S7 and S8 for **ECOF-MnMo$_6$**). Moreover, the vibration band at 2980−2850 $cm^{-1}$ belonging to the $-NH_2$ group of $MnMo_6$-$2NH_2$ obviously decreased (highlighted by a red rectangle); meanwhile the −C═N stretching vibration band at 1625 $cm^{-1}$ became stronger in **TCOF-MnMo$_6$** in comparison to **TCOF**. These results indicated that the amino-functionalized $MnMo_6$ successfully condensed with the subvalent COF and formed a covalent bond linkage (−C═N) between them. In addition, the FTIR spectrum showed that the characteristic peaks, especially the −C═O stretching vibration in **MnMo$_6$@TCOF**, were almost the same as those in TCOF (Figure S7), indicating that no reaction occurred between them. The $N_2$ adsorption capacity and Brunauer−Emmett−Teller (BET) surface area greatly decreased after condensation with $MnMo_6$ (Figure 2e and Figures S9 and S10). These results indicated that POMs successfully filled into the nanopores of the COF. In contrast, the pore size of **MnMo$_6$@TCOF** changed only slightly in comparison to pure the COF (Figure S11), indicating that the pores could not be efficiently loaded with POMs without covalent bonds.

High-resolution XPS measurements for the Mo 3d states of $MnMo_6$-$2NH_2$ and **TCOF-MnMo$_6$/ECOF-MnMo$_6$** were conducted (Figure 2f and Figures S12−S14); the positive shift in the Mo 3d binding energy accounts for the electron transfer on chemical bonding with the COF. The XPS peak of Mo 3d in **MnMo$_6$@TCOF** did not obviously shift in comparison with pure $MnMo_6$ (Figure S15), indicating that there were very few connections (electron migration) between them. No obvious change was found in SEM and TEM (Figures S16−S18), while EDX elemental maps of **TCOF-MnMo$_6$** and **ECOF-MnMo$_6$** signified that Mn and Mo are evenly distributed within these structures (Figure 2g and Figure S19), which demonstrated the homogeneous distribution of POMs in COF substrates. We then conducted solid-state 2D $^1H-^{13}C$ heteronuclear correlation NMR (HET-COR NMR) measurements to further confirm that the polyoxoanions were confined within COF pores. As shown in Figure S20a, the 2D HETCOR spectra of TCOF-$MnMo_6$ exhibit strong cross-signals derived from the C resonance of $MnMo_6$ and the aromatic H of TCOF (highlighted by a red rectangle). The result is caused by an intermolecular dipole interaction, strongly suggesting that the distance between $MnMo_6$ and TCOF is very short and the connection is most likely by bonding. In contrast, when $MnMo_6$ was physically mixed with TCOF, no cross-correlation signals could be found in the 2D $^1H-^{13}C$ HETCOR NMR spectra (Figure S20b), indicating that the distance between nuclei across the heterogeneous interface is greater. These findings directly elucidate that $MnMo_6$ should be predominantly bonded in the pore channels.

There are no peaks of $MnMo_6$ that appear in the PXRD of **COF-POM** (Figures S21 and S22). This indicated that POMs can only exist in the form of single clusters, not aggregated crystals. We found that, after loading of POMs, the diffraction peak of the (100) crystal facet in COF become weaker, which indicated that the extinction effect occurs and further suggests that there is a direct interaction between $MnMo_6$ and the crystal lattice of TCOF. This evidence suggested that the POMs are doped in the COF crystal structure. Due on the size of the POM molecules (8.803 Å), the only possibility is that they are confined in the COF pores. In contrast, the PXRD patterns showed a minor change for **MnMo$_6$@TCOF** (Figure S23), which suggested that the POMs were not effectively doped in the COF crystal structure without covalent linkages. Moreover, the structural integrity of the COF on **COF-POM** could also be verified by $^{13}C$ ssNMR (Figures S24 and S25). The content of $MnMo_6$ in **TCOF-MnMo$_6$** was calculated from an ICP and TGA analysis (Figures S26−S29). The results reveal that the $MnMo_6$ content in the **TCOF-MnMo$_6$** hybrid material is 25.9 wt %, only about half of the theoretical $MnMo_6$ amount for a fully occupied COF (56.6 wt %). In addition to the incomplete reaction, this may also due to a steric hindrance effect: that is, in a straight channel of the 2D COF, the POM single cluster that bonded with the pores on the near surface blocked the subsequent diffusion of the unreacted POMs. More details of the structure and characterization of **TCOF-MnMo$_6$** and **ECOF-MnMo$_6$** are discussed in the Supporting Information.

**Photocatalytic $CO_2$ Reduction Performance.** On the basis of the above illustration of the structure and features of **COF-MnMo$_6$**, it could be proposed that the uniformly distributed $MnMo_6$ will be favorable for full utilization in an application for catalysis. In addition, these COF platforms possess excellent visible light-harvesting ability due to their highly conjugated $\pi$-electron structure, also leading to photoexcited charge delocalization due to the inherent periodic organic building blocks.[51,52] Accordingly, **COF-MnMo$_6$** should be a promising materials platform for photocatalysis. On the


https://doi.org/10.1021/jacs.1c11987
J. Am. Chem. Soc. 2022, 144, 1861−1871

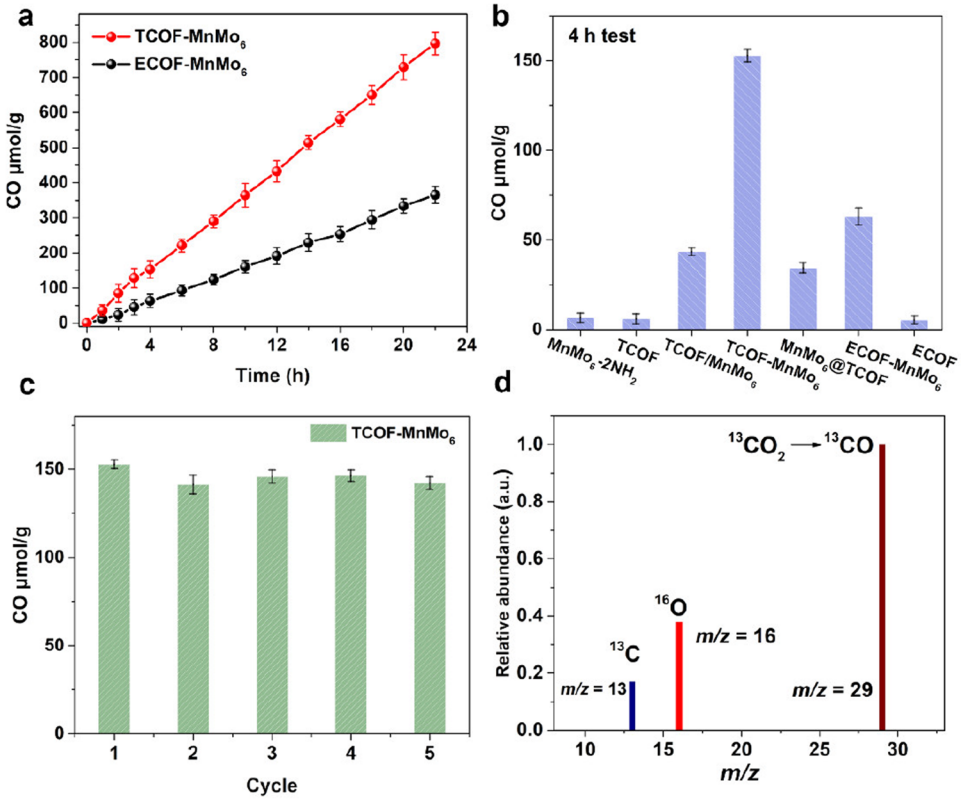


**Figure 3.** Photocatalytic $CO_2$RR performance of **COF-POM**. (a) Time-dependent $CO_2$-to-CO performance for **TCOF-MnMo$_6$** and **ECOF-MnMo$_6$**. (b) Photocatalytic $CO_2$-to-CO performance of **TCOF-MnMo$_6$** in comparison to those of TCOF/MnMo$_6$, MnMo$_6$@TCOF, **ECOF-MnMo$_6$**, and the corresponding building units. (c) Durability measurements of **TCOF-MnMo$_6$** (4 h test). (d) MS spectrum of $^{13}$CO ($m/z$ = 29) produced from the photocatalytic reduction of $^{13}CO_2$.

basis of the above ideas, we then studied the photocatalytic $CO_2$ reduction performance of these **COF-POM** composites. We conducted the $CO_2$ photoreduction tests in a common gas−solid reactor under a $CO_2$ and water vapor atmosphere. It is noted that no additional photosensitizers and sacrificial agents were added. Only CO and $O_2$ were detected as products and were quantified by gas chromatography (details are given in Section S2.1 in the Supporting Information). The highest CO yield was observed in the **TCOF-MnMo$_6$** sample with 796.6 $\mu$mol g$^{-1}$, 2.2 times higher than that of **ECOF-MnMo$_6$** (365.3 $\mu$mol g$^{-1}$) (Figure 3a), and this yield at the forefront of previously reported POM- and COF-based $CO_2$ photoreduction catalysts (Table S1).

We also tested the $CO_2$ photoreduction performance of the building units (raw COF and POM) of these **COF-POM** composites, and the results showed that these building units have barely $CO_2$ to CO transfer activity (Figure 3b). However, after the formation of **COF-POM** composites, in all cases the $CO_2$ reduction activity greatly improved.

More importantly, the covalently linked **TCOF-MnMo$_6$** showed much higher activity in comparison to their physical mixture (**TCOF/MnMo$_6$**, 43.48 $\mu$mol g$^{-1}$) and the **POM@COF** without covalent linkages (**MnMo$_6$@TCOF**, 34.42 $\mu$mol g$^{-1}$) in a 4 h test, proving the superiority of the covalent connection. Additionally, the **TCOF-MnMo$_6$** catalyst can undergo at least five cycles only with little decay in performance (Figure 3c). We then tested the photocatalytic $CO_2$-to-CO yield and production rate for different amounts of **TCOF-MnMo$_6$** in our reactor system. As shown in Figure S30, we found that, with an increase in the catalyst amounts, the CO yield gradually increases; however, the production rate decreases. This may due to a light scattering effect, light shading, and the effective contact area between the catalyst and the light irradiation. For the accurate comparison of photocatalytic activities with those of different laboratories and previously reported data, the apparent quantum efficiency (AQE) for CO evolution was measured at different monochromic light frequencies, and the results are shown in Figure S31. The highest AQE value by **TCOF-MnMo$_6$** for $CO_2$-to-CO at 400 nm is 0.0067%.

The structural integrity of **TCOF-MnMo$_6$** was retained after the reaction, as confirmed by PXRD, FTIR, and XPS characterizations (Figures S32−S34). $^{13}$C isotope labeling experiments were performed to ascertain the carbon sources of photocatalytic products. When a catalytic experiment was performed using $^{13}$C-labeled $CO_2$ ($^{13}CO_2$) as the substrate, $^{13}$CO ($m/z$ = 29) was finally detected by using mass spectrometry, while hardly any $^{12}$CO ($m/z$ = 28) was detected, which confirmed that the produced CO originated from the reactant $CO_2$, ruling out contributions from other carbon-containing species (Figure 3d).

$CO_2$ affinity and optical characterizations, including photoadsorption ability, transient photocurrent response, and a band structure study, were conducted to investigate the internal mechanism of why **COF-POM** composites, especially **TCOF-MnMo$_6$**, had an outstanding photocatalytic $CO_2$ reduction activity. $CO_2$ adsorption ability measurements show that **TCOF-MnMo$_6$** has a higher $CO_2$ uptake (27.01 cm$^3$/g) in comparison to **TCOF** (18.08 cm$^3$/g) (Figure S35). Interestingly, the $CO_2$ uptake of **ECOF-MnMo$_6$** decreased in


https://doi.org/10.1021/jacs.1c11987
J. Am. Chem. Soc. 2022, 144, 1861−1871

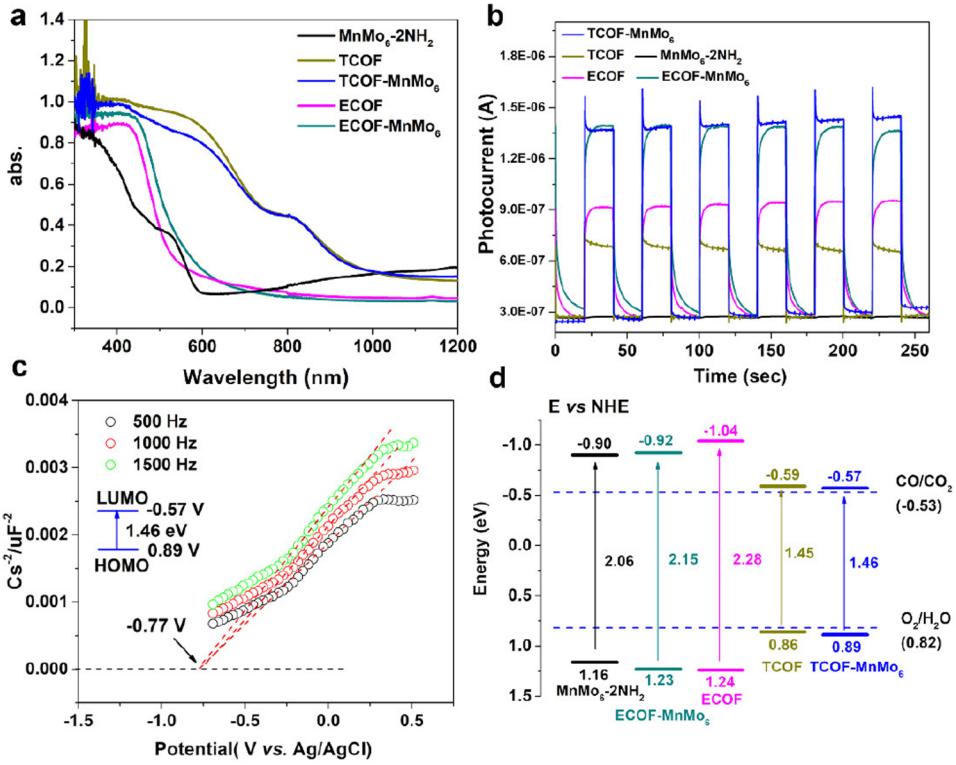


**Figure 4.** Optical characterization of **COF-POM**. (a) Solid-state UV/vis absorption spectra. (b) Transient photocurrent response and (c) Mott–Schottky plot for **TCOF-MnMo$_6$**. (d) Band-structure diagram for **TCOF-MnMo$_6$**, **TCOF**, **ECOF**, **ECOF-MnMo$_6$**, and MnMo$_6$-2NH$_2$.

comparison to **ECOF** (Figure S36), which may be due to the contribution of MnMo$_6$ to $CO_2$ adsorption being offset by the largely reduced surface area. Solid-state UV/vis absorption spectra reveal that **TCOF** and **TCOF-MnMo$_6$** all possess stronger visible light (400–800 nm) absorption capacity in comparison to others (Figure 4a). We conducted photoluminescence (PL) tests for TCOF, MnMo$_6$, **TCOF-MnMo$_6$**, and the physical-mixture composite TCOF/MnMo$_6$ by excitation at 425 nm; the spectra are shown in Figure S37. The PL emission of **TCOF-MnMo$_6$** showed the weakest intensity in comparison to the two building units due to emission quenching, also being much lower than that of the TCOF/MnMo$_6$ mixture (indicating that the nonradiative quenching manner was enhanced due to the formation of an electron-transfer pathway between TCOF and MnMo$_6$ and also demonstrating that the recombination of the photogenerated charges is significantly inhibited). Furthermore, the intensities of the transient photocurrent responses of **TCOF-MnMo$_6$** and **ECOF-MnMo$_6$** were much higher than those of all the building units; this confirms that the covalent link between the two building units greatly enhanced the electronic transfer (Figure 4b). All of the above results suggested that the existence of covalent-bond linkage in a **COF-POM** can lead to superior photoinduced hole–electron separation and transport efficiency.[53−55] Mott–Schottky measurements conjugated with Tauc plots (calculated from UV/vis absorption data, Figures S38–S42) were conducted to determine the optical band structures of **COF-POM** and the corresponding building units (Figure 4c and Figures S43–S46). The LUMO level of **TCOF-MnMo$_6$** is −0.57 eV, and the HOMO level is +0.89 eV. The band-structure diagram for **TCOF-MnMo$_6$**, **TCOF**, **ECOF**, **ECOF-MnMo$_6$**, and **MnMo$_6$-2NH$_2$** are shown in Figure 4d. It is noted that the main structures of the COF and the doped POM single cluster were connected at the molecular level by a covalent bond. Similarly to the element doping of inorganic semiconductors, in the COF-MOF structure, the electronic coupling and redistribution of electrons will occur between these two molecules, thereby forming a new phase with an isolated monolithic or integral semiconductor. Therefore, this molecular-level-linked COF-POM compound can be treated as a molecular catalyst system. Theoretically, a more negative LUMO level in comparison to the $CO_2$/CO standard reduction potential (−0.53 V vs NHE) and a more positive HOMO level in comparison to the $H_2O/O_2$ standard oxidation potential (+0.82 V vs NHE) for a photocatalyst are needed to catalyze the $CO_2$ reduction to CO with $H_2O$ as an electron donor.[49] Interestingly, the band-structure diagram demonstrated that all these COFs, POMs, and **COF-POM**s meet the requirements of the above two half-reactions. Generally speaking, a lower LUMO level (more negative) will result in the photocatalyst possessing a higher thermodynamic overpotential in the catalytic reduction process after excitation, which is more conducive to driving the $CO_2$ reduction reaction. Similarly, a higher HOMO level (or more positive) of the photocatalyst will possess a stronger thermodynamic overpotential for the oxidation reaction. However, for semiconductors, a wider band gap requires higher-energy light irradiation (i.e., shorter-wavelength light) to effectively generate excited electrons. For **ECOF-MnMo$_6$**, which possesses a wider band gap (2.15 eV), higher photo energy is required to effectively excite photoelectrons.[56] In contrast, **TCOF-MnMo$_6$** with a narrow band gap (1.46 eV) can broaden the effective wavelength range and enhance light utilization efficiency. This result explains why **ECOF-MnMo$_6$** exhibits poor photocatalytic performance in comparison to to **TCOF-MnMo$_6$**. Despite this, many thermodynamic (e.g., the


https://doi.org/10.1021/jacs.1c11987
J. Am. Chem. Soc. 2022, 144, 1861−1871

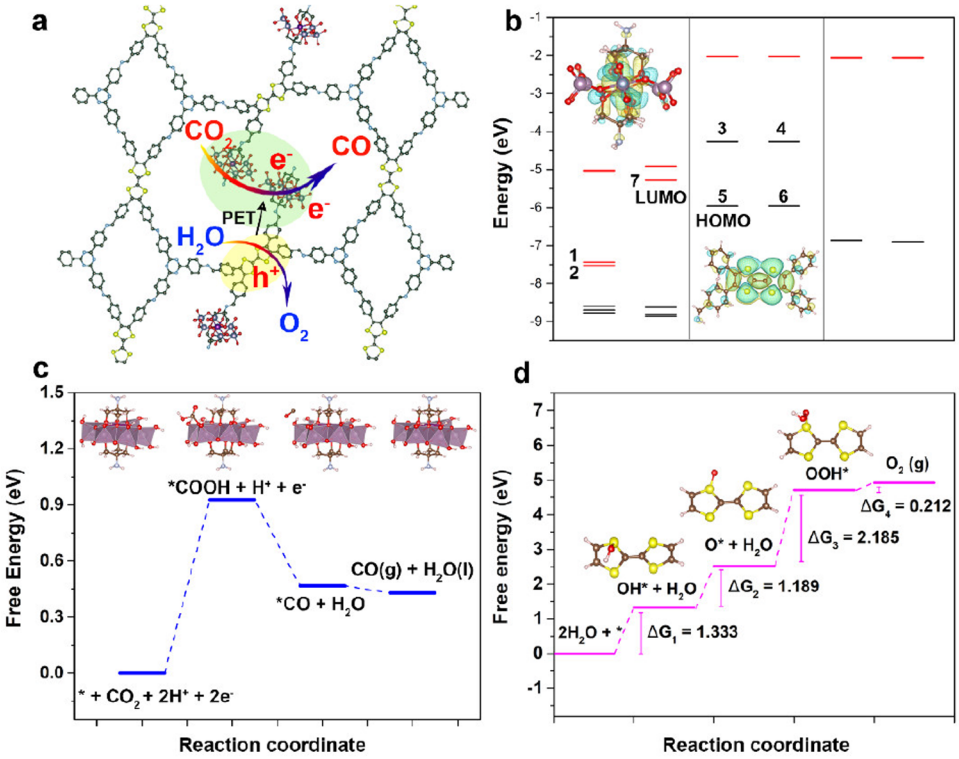


**Figure 5.** Mechanism and DFT calculations. (a) Schematic of the mechanism of **TCOF-MnMo$_6$** for $CO_2$RR coupled with $H_2O$ oxidation. (b) Energy band diagrams for TTF and MnMo$_6$. (c) Free energy diagrams for $CO_2$ reduction to CO on MnMo$_6$ of **TCOF-MnMo$_6$**. (d) Free energy diagrams for $H_2O$ oxidation to $O_2$ on TTF of **TCOF-MnMo$_6$**.

activation energy of $CO_2$ on active sites) and kinetic factors (e.g., the diffusion rates of $CO_2$ and $H_2O$, electron transport rates, and so on) collaboratively determined the final photocatalytic $CO_2$ reduction performance.[57] Hence, a more careful study is still needed in subsequent work. In this work, we studied in detail the three most important factors, that is, light absorption capacity, photoinduced electron separation or transport efficiency, and band structure, to illustrate the reasons for the performance variation found experimentally. Overall, the above results indicate that **TCOF-MnMo$_6$** has an optimal $CO_2$ reduction activity, which is consistent with the performance test results.

**Investigating Structure−Function Relationships.** On the basis of the above experiments and analysis, an intrinsic mechanism was proposed to explain the $CO_2$ reduction with an $H_2O$ oxidation process for **TCOF-MnMo$_6$** (Figure 5a): under visible light irradiation, the photogenerated excited electrons and holes separated, and then electrons transfer from the TTF moiety of **TCOF** (HOMO center) to the MnMo$_6$ moiety (LUMO center) through a PET process, followed by a move to the catalytically active sites in MnMo$_6$ for $CO_2$ reduction. Meanwhile, the photogenerated holes in TTF are capable of oxidizing $H_2O$ to $O_2$, by which the catalytic system gains electrons from $H_2O$ (as electron donor) to keep the charge balance.

In view of the precise structure of **COF-POM**, DFT calculations were conducted to gain insights into the thermodynamics of the $CO_2$ reduction and $H_2O$ oxidation process. The PET process driven by light irradiation was studied by an orbital analysis, in particular the energy levels of the HOMO and LUMO that determine the first excitation. Specifically, for **TCOF-MnMo$_6$**, the molecular orbital energy levels of MnMo$_6$, TTF, and TAPT were calculated and are shown in Figure 5b.

In all of these energy level schemes, the occupied and unoccupied orbitals are indicated by black and red lines, respectively. For **TCOF-MnMo$_6$**, we found the LUMO level of MnMo$_6$ is lower than the HOMO level of both TTF and TAPT; therefore, for a hybrid of these three monomers, the electron in the HOMO of TTF and TAPT, i.e. orbital s3 and 4 within the green dashed framework on TTF, will spontaneously transition to orbitals 1 and 2 in MnMo$_6$. As a result, the HOMO and LUMO of hybrid structures become orbitals 5 and 6 on TTF and orbital 7 on MnMo$_6$, and the LUMO−HOMO gap is determined to be 0.68 eV. Thus, on stimulation by light, photogenerated electrons will transfer to MnMo$_6$ for $CO_2$ reduction, leaving photogenerated positive holes in TTF for $H_2O$ oxidation.

The calculated free energy diagram for the $CO_2$ reduction process is given in Figure 5c. The proton-coupled electron transfer step to generate *COOH from the adsorbed $CO_2$ serves as the potential-determining step (PDS), corresponding to 0.9 eV for MnMo$_6$. In the case of $H_2O$ oxidation, on the basis of previous work by our group,[49] for the hole-doped TTF fragment, the spin density is mostly located on the linker C═C and the S atoms, indicating that the $H_2O$ oxidation process can be conducted on both sites (Figure 5d and Figure S52). The $H_2O$ oxidation process on the $[TTF]^+$ fragment can be divided into four steps (Section S4.4 in the Supporting Information): the dissociation of a water molecule into an OH group, which is adsorbed on the catalyst surface (*OH), the dissociation of *OH into O (*O), the reaction of *O with another $H_2O$ molecule leading to an OOH group (*OOH), and the formation of $O_2$. In both active sites on either C or S,


https://doi.org/10.1021/jacs.1c11987
J. Am. Chem. Soc. 2022, 144, 1861−1871

the third step, where an adsorbed O atom reacts with an $H_2O$ molecule to form *OOH, is the potential-determining step.

## ■ CONCLUSIONS

In conclusion, our work developed a general method for uniformly confining POM clusters in COF pores. The **TCOF-MnMo$_6$** as photocatalyst showed excellent activity for $CO_2$ reduction to CO with 37.25 $\mu$mol $g^{-1}$ $h^{-1}$ and ca. 100% selectivity. We demonstrated that the covalently bonded COF and POM combined light absorption, electron transfer, and suitable band gap and active sites for visible light catalytic $CO_2$ reduction and $H_2O$ oxidation with high activity. Furthermore, a DFT simulation demonstrated that the PET process occurs from the COF to the POM, and then $CO_2$ reduction and $H_2O$ oxidation occurred, respectively. We believe that our developed method has a great potential to solve the stability and efficiency issues of cluster-based catalysts. More importantly, this work provides new insight into the design and development of supported metal cluster (such as metal halide clusters, metal sulfide clusters, metalloid clusters, and so on) based catalysts.

## ■ ASSOCIATED CONTENT

### Supporting Information

The Supporting Information is available free of charge at https://pubs.acs.org/doi/10.1021/jacs.1c11987.

Detailed information regarding the experimental methods, characterization analysis, DFT calculations, and simulation of the theoretical COF structure (PDF)

### Accession Codes

CCDC 2074257−2074259 contain the supplementary crystallographic data for this paper. These data can be obtained free of charge via www.ccdc.cam.ac.uk/data_request/cif, or by emailing data_request@ccdc.cam.ac.uk, or by contacting The Cambridge Crystallographic Data Centre, 12 Union Road, Cambridge CB2 1EZ, UK; fax: +44 1223 336033.

## ■ AUTHOR INFORMATION


### Corresponding Author

**Ya-Qian Lan** − *School of Chemistry, South China Normal University, Guangzhou 510006, People's Republic of China; Jiangsu Collaborative Innovation Centre of Biomedical Functional Materials, Jiangsu Key Laboratory of New Power Batteries, School of Chemistry and Materials Science, Nanjing Normal University, Nanjing 210023, People's Republic of China;* orcid.org/0000-0002-2140-7980; Email: yqlan@m.scnu.edu.cn, yqlan@njnu.edu.cn

### Authors

**Meng Lu** − *School of Chemistry, South China Normal University, Guangzhou 510006, People's Republic of China*

**Mi Zhang** − *School of Chemistry, South China Normal University, Guangzhou 510006, People's Republic of China*

**Jiang Liu** − *School of Chemistry, South China Normal University, Guangzhou 510006, People's Republic of China; Jiangsu Collaborative Innovation Centre of Biomedical Functional Materials, Jiangsu Key Laboratory of New Power Batteries, School of Chemistry and Materials Science, Nanjing Normal University, Nanjing 210023, People's Republic of China*

**Tao-Yuan Yu** − *Jiangsu Collaborative Innovation Centre of Biomedical Functional Materials, Jiangsu Key Laboratory of New Power Batteries, School of Chemistry and Materials Science, Nanjing Normal University, Nanjing 210023, People's Republic of China*

**Jia-Nan Chang** − *Jiangsu Collaborative Innovation Centre of Biomedical Functional Materials, Jiangsu Key Laboratory of New Power Batteries, School of Chemistry and Materials Science, Nanjing Normal University, Nanjing 210023, People's Republic of China*

**Lin-Jie Shang** − *Jiangsu Collaborative Innovation Centre of Biomedical Functional Materials, Jiangsu Key Laboratory of New Power Batteries, School of Chemistry and Materials Science, Nanjing Normal University, Nanjing 210023, People's Republic of China*

**Shun-Li Li** − *Jiangsu Collaborative Innovation Centre of Biomedical Functional Materials, Jiangsu Key Laboratory of New Power Batteries, School of Chemistry and Materials Science, Nanjing Normal University, Nanjing 210023, People's Republic of China; School of Chemistry, South China Normal University, Guangzhou 510006, People's Republic of China*

Complete contact information is available at: https://pubs.acs.org/10.1021/jacs.1c11987


### Author Contributions

All authors have approved the final version of the manuscript.

### Notes

The authors declare no competing financial interest.

## ■ ACKNOWLEDGMENTS

This work was financially supported by the NSFC (Nos. 21871141, 21871142, 21701085, 21901122, and 22105080), the NSF of Jiangsu Province of China (No. BK20171032), the Natural Science Research of Jiangsu Higher Education Institutions of China (Nos. 17KJB150025 and 19KJB150011) and Project funded by the China Postdoctoral Science Foundation (Nos. 2020M682747 and 2021M701270), and the Priority Academic Program Development of Jiangsu Higher Education Institutions and the Foundation of Jiangsu Collaborative Innovation Center of Biomedical Functional Materials. We acknowledge the Shenzhen HUASUAN technicians for assistance with theoretical calculations.

## ■ REFERENCES


(1) Liu, L.; Corma, A. Metal Catalysts for Heterogeneous Catalysis: From Single Atoms to Nanoclusters and Nanoparticles. *Chem. Rev.* **2018**, *118* (10), 4981−5079.

(2) Lu, Y.; Chen, W. Sub-nanometre sized metal clusters: from synthetic challenges to the unique property discoveries. *Chem. Soc. Rev.* **2012**, *41* (9), 3594−3623.

(3) Ye, R.; Zhukhovitskiy, A. V.; Deraedt, C. V.; Toste, F. D.; Somorjai, G. A. Supported Dendrimer-Encapsulated Metal Clusters: Toward Heterogenizing Homogeneous Catalysts. *Acc. Chem. Res.* **2017**, *50* (8), 1894−1901.

(4) Liu, Q.; Wang, X. Polyoxometalate Clusters: Sub-nanometer Building Blocks for Construction of Advanced Materials. *Matter* **2020**, *2* (4), 816−841.

(5) Miras, H. N.; Yan, J.; Long, D.-L.; Cronin, L. Engineering polyoxometalates with emergent properties. *Chem. Soc. Rev.* **2012**, *41* (22), 7403.

(6) Liu, Q.; Zhang, W. H.; Lang, J. P. Versatile thiomolybdate-(thiotungstate)-copper-sulfide clusters and multidimensional polymers linked by cyanides. *Coord. Chem. Rev.* **2017**, *350*, 248−274.

(7) Han, X.-B.; Li, Y.-G.; Zhang, Z.-M.; Tan, H.-Q.; Lu, Y.; Wang, E.-B. Polyoxometalate-Based Nickel Clusters as Visible Light-Driven

Water Oxidation Catalysts. *J. Am. Chem. Soc.* **2015**, *137* (16), 5486−5493.
(8) Qiao, B.; Wang, A.; Yang, X.; Allard, L. F.; Jiang, Z.; Cui, Y.; Liu, J.; Li, J.; Zhang, T. Single-atom catalysis of CO oxidation using Pt1/FeOx. *Nat. Chem.* **2011**, *3* (8), 634−641.
(9) Dong, C.; Li, Y.; Cheng, D.; Zhang, M.; Liu, J.; Wang, Y.-G.; Xiao, D.; Ma, D. Supported Metal Clusters: Fabrication and Application in Heterogeneous Catalysis. *ACS Catal.* **2020**, *10* (19), 11011−11045.
(10) Liu, L.; Corma, A. Confining isolated atoms and clusters in crystalline porous materials for catalysis. *Nat. Rev.Mater.* **2021**, *6* (3), 244−263.
(11) Wang, Y.; Su, H.; He, Y.; Li, L.; Zhu, S.; Shen, H.; Xie, P.; Fu, X.; Zhou, G.; Feng, C.; Zhao, D.; Xiao, F.; Zhu, X.; Zeng, Y.; Shao, M.; Chen, S.; Wu, G.; Zeng, J.; Wang, C. Advanced Electrocatalysts with Single-Metal-Atom Active Sites. *Chem. Rev.* **2020**, *120* (21), 12217−12314.
(12) Liu, C.; Li, H.; Liu, F.; Chen, J.; Yu, Z.; Yuan, Z.; Wang, C.; Zheng, H.; Henkelman, G.; Wei, L.; Chen, Y. Intrinsic Activity of Metal Centers in Metal−Nitrogen−Carbon Single-Atom Catalysts for Hydrogen Peroxide Synthesis. *J. Am. Chem. Soc.* **2020**, *142* (52), 21861−21871.
(13) Xia, B.; Zhang, Y.; Ran, J.; Jaroniec, M.; Qiao, S.-Z. Single-Atom Photocatalysts for Emerging Reactions. *ACS Central Science* **2021**, *7* (1), 39−54.
(14) Liu, J.; Cao, D.; Xu, H.; Cheng, D. From double-atom catalysts to single-cluster catalysts: A new frontier in heterogeneous catalysis. *Nano Select* **2021**, *2* (2), 251−270.
(15) Serna, P.; Gates, B. C. Molecular Metal Catalysts on Supports: Organometallic Chemistry Meets Surface Science. *Acc. Chem. Res.* **2014**, *47* (8), 2612−2620.
(16) Tang, Y.-J.; Gao, M.-R.; Liu, C.-H.; Li, S.-L.; Jiang, H.-L.; Lan, Y.-Q.; Han, M.; Yu, S.-H. Porous Molybdenum-Based Hybrid Catalysts for Highly Efficient Hydrogen Evolution. *Angew. Chem., Int. Ed.* **2015**, *54* (44), 12928−12932.
(17) Kawasaki, N.; Wang, H.; Nakanishi, R.; Hamanaka, S.; Kitaura, R.; Shinohara, H.; Yokoyama, T.; Yoshikawa, H.; Awaga, K. Nanohybridization of Polyoxometalate Clusters and Single-Wall Carbon Nanotubes: Applications in Molecular Cluster Batteries. *Angew. Chem., Int. Ed.* **2011**, *50* (15), 3471−3474.
(18) Ji, Y.; Huang, L.; Hu, J.; Streb, C.; Song, Y.-F. Polyoxometalate-functionalized nanocarbon materials for energy conversion, energy storage and sensor systems. *Energy Environ. Sci.* **2015**, *8* (3), 776−789.
(19) Zhang, Y.; Liu, J.; Li, S.-L.; Su, Z.-M.; Lan, Y.-Q. Polyoxometalate-based materials for sustainable and clean energy conversion and storage. *EnergyChem.* **2019**, *1* (3), 100021.
(20) Lv, H.; Guo, W.; Wu, K.; Chen, Z.; Bacsa, J.; Musaev, D. G.; Geletii, Y. V.; Lauinger, S. M.; Lian, T.; Hill, C. L. A noble-metal-free, tetra-nickel polyoxotungstate catalyst for efficient photocatalytic hydrogen evolution. *J. Am. Chem. Soc.* **2014**, *136* (40), 14015−14018.
(21) Zhang, Z.-M.; Zhang, T.; Wang, C.; Lin, Z.; Long, L.-S.; Lin, W. Photosensitizing Metal−Organic Framework Enabling Visible-Light-Driven Proton Reduction by a Wells−Dawson-Type Polyoxometalate. *J. Am. Chem. Soc.* **2015**, *137* (9), 3197−3200.
(22) Han, X.-B.; Zhang, Z.-M.; Zhang, T.; Li, Y.-G.; Lin, W.; You, W.; Su, Z.-M.; Wang, E.-B. Polyoxometalate-Based Cobalt−Phosphate Molecular Catalysts for Visible Light-Driven Water Oxidation. *J. Am. Chem. Soc.* **2014**, *136* (14), 5359−5366.
(23) Tian, J.; Xu, Z.-Y.; Zhang, D.-W.; Wang, H.; Xie, S.-H.; Xu, D.-W.; Ren, Y.-H.; Wang, H.; Liu, Y.; Li, Z.-T. Supramolecular metal-organic frameworks that display high homogeneous and heterogeneous photocatalytic activity for $H_2$ production. *Nat. Commun.* **2016**, *7* (1), 11580.
(24) Cao, Y.; Chen, Q.; Shen, C.; He, L. Polyoxometalate-Based Catalysts for CO2 Conversion. *Molecules* **2019**, *24* (11), 2069.
(25) Xie, S.-L.; Liu, J.; Dong, L.-Z.; Li, S.-L.; Lan, Y.-Q.; Su, Z.-M. Hetero-metallic active sites coupled with strongly reductive polyoxometalate for selective photocatalytic $CO_2$-to-$CH_4$ conversion in water. *Chem. Sci.* **2019**, *10* (1), 185−190.
(26) Ettedgui, J.; Diskin-Posner, Y.; Weiner, L.; Neumann, R. Photoreduction of Carbon Dioxide to Carbon Monoxide with Hydrogen Catalyzed by a Rhenium(I) Phenanthroline−Polyoxometalate Hybrid Complex. *J. Am. Chem. Soc.* **2011**, *133* (2), 188−190.
(27) Benseghir, Y.; Lemarchand, A.; Duguet, M.; Mialane, P.; Gomez-Mingot, M.; Roch-Marchal, C.; Pino, T.; Ha-Thi, M.-H.; Haouas, M.; Fontecave, M.; Dolbecq, A.; Sassoye, C.; Mellot-Draznieks, C. Co-immobilization of a Rh Catalyst and a Keggin Polyoxometalate in the UiO-67 Zr-Based Metal−Organic Framework: In Depth Structural Characterization and Photocatalytic Properties for $CO_2$ Reduction. *J. Am. Chem. Soc.* **2020**, *142* (20), 9428−9438.
(28) Li, N.; Liu, J.; Liu, J. J.; Dong, L. Z.; Li, S. L.; Dong, B. X.; Kan, Y. H.; Lan, Y. Q. Self-Assembly of a Phosphate-Centered Polyoxo-Titanium Cluster: Discovery of the Heteroatom Keggin Family. *Angew. Chem., Int. Ed.* **2019**, *58* (48), 17260−17264.
(29) Yang, H.; Yang, D.; Wang, X. POM-Incorporated CoO Nanowires for Enhanced Photocatalytic Syngas Production from $CO_2$. *Angew. Chem., Int. Ed.* **2020**, *59* (36), 15527−15531.
(30) Li, X. H.; He, P.; Wang, T.; Zhang, X. W.; Chen, W. L.; Li, Y. G. Keggin-Type Polyoxometalate-Based ZIF-67 for Enhanced Photocatalytic Nitrogen Fixation. *ChemSusChem* **2020**, *13* (10), 2769−2778.
(31) Quattrini, M. C.; Fujii, S.; Yamada, K.; Fukuyama, T.; Ravelli, D.; Fagnoni, M.; Ryu, I. Versatile cross-dehydrogenative coupling of heteroaromatics and hydrogen donors via decatungstate photocatalysis. *Chem. Commun.* **2017**, *53* (15), 2335−2338.
(32) Suzuki, K.; Mizuno, N.; Yamaguchi, K. Polyoxometalate Photocatalysis for Liquid-Phase Selective Organic Functional Group Transformations. *ACS Catal.* **2018**, *8* (11), 10809−10825.
(33) Li, N.; Liu, J.; Dong, B. X.; Lan, Y. Q. Polyoxometalate-Based Compounds for Photo-and Electrocatalytic Applications. *Angew. Chem., Int. Ed.* **2020**, *59* (47), 20779−20793.
(34) Gumerova, N. I.; Rompel, A. Synthesis, structures and applications of electron-rich polyoxometalates. *Nature Reviews Chemistry* **2018**, *2*, 0112.
(35) Diercks, C. S.; Liu, Y.; Cordova, K. E.; Yaghi, O. M. The role of reticular chemistry in the design of $CO_2$ reduction catalysts. *Nat. Mater.* **2018**, *17* (4), 301−307.
(36) Liu, J.; Shi, W.; Ni, B.; Yang, Y.; Li, S.; Zhuang, J.; Wang, X. Incorporation of clusters within inorganic materials through their addition during nucleation steps. *Nat. Chem.* **2019**, *11* (9), 839−845.
(37) Li, X.; Cai, S.; Sun, B.; Yang, C.; Zhang, J.; Liu, Y. Chemically Robust Covalent Organic Frameworks: Progress and Perspective. *Matter* **2020**, *3* (5), 1507−1540.
(38) Liu, R.; Tan, K. T.; Gong, Y.; Chen, Y.; Li, Z.; Xie, S.; He, T.; Lu, Z.; Yang, H.; Jiang, D. Covalent organic frameworks: an ideal platform for designing ordered materials and advanced applications. *Chem. Soc. Rev.* **2021**, *50* (1), 120−242.
(39) Liang, R.-R.; Jiang, S.-Y.; A, R.-H.; Zhao, X. Two-dimensional covalent organic frameworks with hierarchical porosity. *Chem. Soc. Rev.* **2020**, *49* (12), 3920−3951.
(40) Wang, Z.; Zhang, S.; Chen, Y.; Zhang, Z.; Ma, S. Covalent organic frameworks for separation applications. *Chem. Soc. Rev.* **2020**, *49* (3), 708−735.
(41) Ma, H.; Liu, B.; Li, B.; Zhang, L.; Li, Y. G.; Tan, H. Q.; Zang, H. Y.; Zhu, G. Cationic Covalent Organic Frameworks: A Simple Platform of Anionic Exchange for Porosity Tuning and Proton Conduction. *J. Am. Chem. Soc.* **2016**, *138* (18), 5897−5903.
(42) Chen, X.; Geng, K.; Liu, R.; Tan, K. T.; Gong, Y.; Li, Z.; Tao, S.; Jiang, Q.; Jiang, D. Covalent Organic Frameworks: Chemical Approaches to Designer Structures and Built-In Functions. *Angew. Chem., Int. Ed.* **2020**, *59* (13), 5050−5091.
(43) Lu, M.; Zhang, M.; Liu, C.-G.; Liu, J.; Shang, L.-J.; Wang, M.; Chang, J.-N.; Li, S.-L.; Lan, Y.-Q. Stable Dioxin-Linked Metallophthalocyanine Covalent Organic Frameworks (COFs) as Photo-Coupled Electrocatalysts for $CO_2$ Reduction. *Angew. Chem., Int. Ed.* **2021**, *60* (9), 4864−4871.
(44) Banerjee, T.; Haase, F.; Trenker, S.; Biswal, B. P.; Savasci, G.; Duppel, V.; Moudrakovski, I.; Ochsenfeld, C.; Lotsch, B. V. Sub-

stoichiometric 2D covalent organic frameworks from tri- and tetratopic linkers. *Nat. Commun.* **2019**, *10* (1), 2689.
(45) Xiong, Y.; Liao, Q.; Huang, Z.; Huang, X.; Ke, C.; Zhu, H.; Dong, C.; Wang, H.; Xi, K.; Zhan, P.; Xu, F.; Lu, Y. Ultrahigh Responsivity Photodetectors of 2D Covalent Organic Frameworks Integrated on Graphene. *Adv. Mater.* **2020**, *32* (9), 1907242.
(46) Liao, Q.; Xu, W.; Huang, X.; Ke, C.; Zhang, Q.; Xi, K.; Xie, J. Donor-acceptor type [4 + 3] covalent organic frameworks: sub-stoichiometric synthesis and photocatalytic application. *Science China Chemistry* **2020**, *63* (5), 707−714.
(47) Xu, W.; Pei, X.; Diercks, C. S.; Lyu, H.; Ji, Z.; Yaghi, O. M. A Metal−Organic Framework of Organic Vertices and Polyoxometalate Linkers as a Solid-State Electrolyte. *J. Am. Chem. Soc.* **2019**, *141* (44), 17522−17526.
(48) Song, Y.-F.; McMillan, N.; Long, D.-L.; Kane, S.; Malm, J.; Riehle, M. O.; Pradeep, C. P.; Gadegaard, N.; Cronin, L. Micropatterned Surfaces with Covalently Grafted Unsymmetrical Polyoxometalate-Hybrid Clusters Lead to Selective Cell Adhesion. *J. Am. Chem. Soc.* **2009**, *131* (4), 1340−1341.
(49) Lu, M.; Liu, J.; Li, Q.; Zhang, M.; Liu, M.; Wang, J.-L.; Yuan, D.-Q.; Lan, Y.-Q. Rational Design of Crystalline Covalent Organic Frameworks for Efficient $CO_2$ Photoreduction with $H_2O$. *Angew. Chem., Int. Ed.* **2019**, *58* (36), 12392−12397.
(50) Nguyen, H. L.; Gropp, C.; Ma, Y.; Zhu, C.; Yaghi, O. M. 3D Covalent Organic Frameworks Selectively Crystallized through Conformational Design. *J. Am. Chem. Soc.* **2020**, *142* (48), 20335−20339.
(51) Zhong, W.; Sa, R.; Li, L.; He, Y.; Li, L.; Bi, J.; Zhuang, Z.; Yu, Y.; Zou, Z. A Covalent Organic Framework Bearing Single Ni Sites as a Synergistic Photocatalyst for Selective Photoreduction of $CO_2$ to CO. *J. Am. Chem. Soc.* **2019**, *141* (18), 7615−7621.
(52) Gong, Y. N.; Zhong, W.; Li, Y.; Qiu, Y.; Zheng, L.; Jiang, J.; Jiang, H. L. Regulating Photocatalysis by Spin-State Manipulation of Cobalt in Covalent Organic Frameworks. *J. Am. Chem. Soc.* **2020**, *142* (39), 16723−16731.
(53) Zhang, M.; Lu, M.; Lang, Z.-L.; Liu, J.; Liu, M.; Chang, J.-N.; Li, L.-Y.; Shang, L.-J.; Wang, M.; Li, S.-L.; Lan, Y.-Q. Semiconductor/Covalent-Organic-Framework Z-Scheme Heterojunctions for Artificial Photosynthesis. *Angew. Chem., Int. Ed.* **2020**, *59* (16), 6500−6506.
(54) Zhao, G.; Pang, H.; Liu, G.; Li, P.; Liu, H.; Zhang, H.; Shi, L.; Ye, J. Co-porphyrin/carbon nitride hybrids for improved photocatalytic CO2 reduction under visible light. *Applied Catalysis B: Environmental* **2017**, *200*, 141−149.
(55) Ma, B.; Chen, G.; Fave, C.; Chen, L.; Kuriki, R.; Maeda, K.; Ishitani, O.; Lau, T.-C.; Bonin, J.; Robert, M. Efficient Visible-Light-Driven $CO_2$ Reduction by a Cobalt Molecular Catalyst Covalently Linked to Mesoporous Carbon Nitride. *J. Am. Chem. Soc.* **2020**, *142* (13), 6188−6195.
(56) Voiry, D.; Shin, H. S.; Loh, K. P.; Chhowalla, M. Low-dimensional catalysts for hydrogen evolution and $CO_2$ reduction. *Nature Reviews Chemistry* **2018**, *2*, 0105.
(57) White, J. L.; Baruch, M. F.; Pander, J. E., Iii; Hu, Y.; Fortmeyer, I. C.; Park, J. E.; Zhang, T.; Liao, K.; Gu, J.; Yan, Y.; Shaw, T. W.; Abelev, E.; Bocarsly, A. B. Light-Driven Heterogeneous Reduction of Carbon Dioxide: Photocatalysts and Photoelectrodes. *Chem. Rev.* **2015**, *115* (23), 12888−935.





https://doi.org/10.1021/jacs.1c11987
J. Am. Chem. Soc. 2022, 144, 1861−1871